Progressive microscopic damage associated with fault growth

T. Tamarkin,[1] A. Ougier-Simonin,[1] and Wenlu Zhu[1]

Received 24 May 2012; revised 20 June 2012; accepted 25 June 2012; published 3 August 2012.

[1] It is known that microstuctural damage precedes macroscopic fracture in rocks during brittle failure. The quantitative relationship between the grain-scale damage and fault growth is not yet clearly understood, partly due to the unstable nature of the faulting process. A lateral relaxation path was devised so that a rock sample can be deformed to failure by increasing differential stress along with decreasing effective mean stress. Porous rocks subjected to such a loading path exhibit a rather stable fault growth. Microstructural damage was analyzed on samples deformed to various post-yielding stages before macroscopic faulting emerges. The intensity of microcracking is strain rate and effective pressure dependent. At peak stress, no spatial correlation among the regions with high crack intensities was observed. Beyond peak stress, the overall crack intensity increases and the regions with high crack intensities coalesce to form a macroscopic fracture. These results provide constraints for a better understanding of fault rupture. **Citation:** Tamarkin, T., A. Ougier-Simonin, and W. Zhu (2012), Progressive microscopic damage associated with fault growth, *Geophys. Res. Lett.*, *39*, L15303, doi:10.1029/2012GL052487.

1. Introduction

[2] Seismogenic faulting is generally referred to rupture of a fault accompanied by a sudden release of elastic energy, which causes earthquakes [e.g., *Reid*, 1910; *Scholz*, 2002]. The precursory phenomena that precede seismogenic faulting generate lots of attention because of their potential importance in earthquake mitigation. For instance, *Scholz et al.* [1973] reported that the radon content in deep well water in Blue Mountain Lake, New York, increased several folds prior to the 1971 earthquake swarm. It has been postulated that in response to tectonic stresses, fault rocks dilate due to opening up of cracks in their interior, and crack opening releases radon gas in this region and the process continues until seismogenic fault rupture occurs. Better assessments of various precursory phenomena and their applications in earthquake predictions require quantitative knowledge of the rupture process.

[3] Due to their close correlation to earthquake nucleation and generation, quantitative understanding of the nucleation and propagation of faults has been an important subject in experimental rock deformation [e.g., *Scholz*, 2002]. Typically, a deformation experiment is conducted under conventional compressive loading, in which a cylindrical sample is subjected to increasing stress along its axial direction (via a loading frame advanced at constant displacement rate) and the radial stresses are kept constant (Figure 1a). Using this loading configuration, the elastic energy stored in the loading frame and the sample increases continuously during deformation. At failure, the high elastic energy stored in both the loading frame and the sample facilitates unstable fault growth [e.g., *Jaeger and Cook*, 1976].

[4] Several attempts were made to increase the stability during fault growth in order to observe the failure process in details. The main idea is to increase the stiffness of the loading frame to reduce the elastic energy available at failure [e.g., *Wawersik and Brace*, 1971; *Wong*, 1982]. Alternatively, stable fault growth can be achieved by using load-control feedback to arrest unstable fault development during failure [e.g., *Terada et al.*, 1984; *Lockner et al.*, 1992]. In a seminal study, *Lockner et al.* [1992] designed an axial displacement feedback system to maintain constant acoustic emission (AE) rate, i.e., a sudden increase in AE activity would trigger rapid unloading and thus stabilize fracture propagation. This approach led to a quasistatic fault growth in both granite and sandstone samples, which enabled a successful continuous recording of AE locations that mark the sites where microscopic damage took place [*Lockner et al.*, 1992]. Using AE as a proxy of microcracking, *Lockner et al.* [1992] provided the first systematic 3-dimensional view on how microscopic damage nucleates, coalesces and forms macroscopic fractures.

[5] In this study, we took a different approach to stabilize fault growth and investigated the prefaulting microscopic damage of porous sandstones. Unlike in previous studies [i.e., *Wawersik and Brace*, 1971; *Lockner et al.*, 1992], sandstone samples were deformed under a different loading configuration. Using this so-called lateral relaxation loading path, a rock sample is subjected to decreasing radial stresses and the axial stress is kept constant (Figure 1a). The two servo-controlled triaxial testing machines used in this study are relatively stiff (with apparent stiffness of $\sim 5 \times 10^7$ and 2×10^8 N/m, respectively). To maintain a constant axial stress, the machine axial displacement during the lateral relaxation loading is significantly smaller than that during the conventional loading (Figure 1b). As a result, the elastic energy stored in the loading frame during a lateral relaxation experiment (proportional to the area under the red line in Figure 1b) is significantly smaller than that in a conventional compression test (i.e., area under the black line in Figure 1b). Using the new loading configuration, the effective machine stiffness more than doubles the apparent machine stiffness (Figure 1b), which leads to enhanced post-failure stability. While the reduction in elastic energy stored in the loading frame alone is not sufficient to change the post-failure behavior of rocks such as granites because the elastic energy stored in these rocks is high enough to lead to unstable fault growth, this approach provides enhanced stability for studying the post-failure fault growth in porous

[1]Department of Geology, University of Maryland, College Park, Maryland, USA.

Corresponding author: W. Zhu, Department of Geology, University of Maryland, College Park, MD 20742, USA. (wzhu@umd.edu)

0094-8276/12/2012GL052487

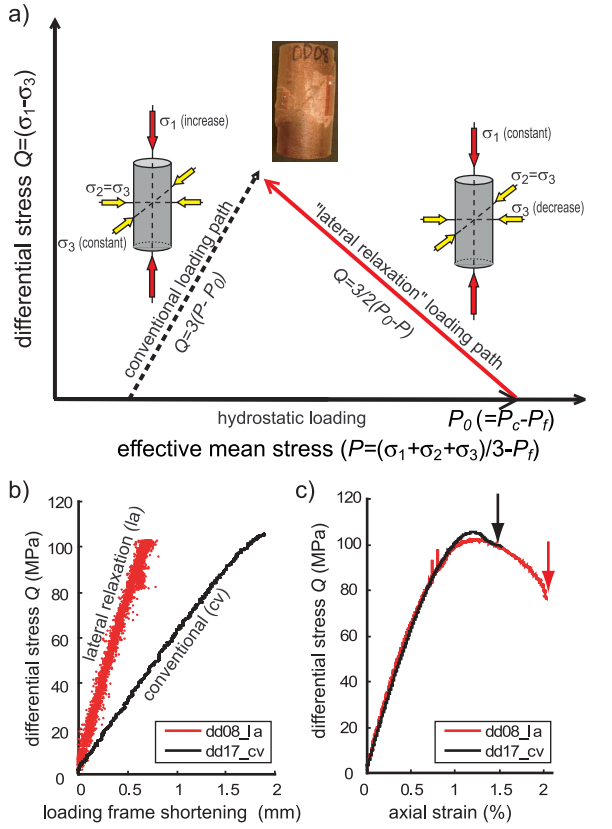

Figure 1. (a) Comparison of a conventional loading path (dashed line) to the new lateral relaxation loading path (solid line) used in this study. Schematic diagrams of the sample stress states during loading are shown. During conventional loading, axial stress σ_1 (red arrows) increases with constant radial stresses $\sigma_2 = \sigma_3$ (yellow arrows). During lateral relaxation loading, radial stresses $\sigma_2 = \sigma_3$ decrease with constant axial stress σ_1. To achieve the same yield stress using these 2 different loading paths, deformation has to start at different effective pressures P_0. A picture of a deformed sample dd08 is shown as an insert. A sharp shear fracture and the 2 strain gauges are observed. (b) The shortening of the loading frame during deformation before peak stress was attained. The red line represents data obtained using the lateral relaxation loading path, the black line represents data from a conventional test. Elastic energy stored in the loading frame is considerably smaller during the relaxation experiment (area under the red line) than that during the conventional loading (area under the black line). (c) Comparison of the stress-strain curves of sample dd08 deformed at a constant strain rate of 5×10^{-6}/s and an effective pressure of 190 MPa using a lateral relaxation path (red) and sample dd17 deformed at the same strain rate and an effective pressure of 70 MPa using a conventional loading path (black). Arrows indicate the loss of strain gauge(s) by a through-going shear fracture. It is clear to that the new loading method provides a larger window to study the inelastic behavior between the peak stress and a fully developed shear fracture.

sandstones (Figure 1c). Using this loading configuration, the strain rate in a deformation test can be kept constant, which minimizes the uncertainties in microstructural damage related to cyclic loading (i.e., unload-reload) as in the feedback load control approach [i.e., *Lockner et al.*, 1992].

[6] A suite of porous sandstone samples were deformed and subsequently unloaded at different post-yield failure stages. Progressive microstructural damage in these samples was analyzed via quantitative characterization of crack damage indices and crack density. The results contribute to an improved understanding of the relationship between microscopic damage and macroscopic fault development, which is pertinent to earthquake nucleation process.

2. Experimental Setup

[7] In a conventional triaxial compression test, a rock sample is first compressed hydrostatically to a preset confining pressure P_c (i.e., $\sigma_1 = \sigma_2 = \sigma_3 = P_c$), where σ_1, σ_2, and σ_3, are maximum, intermediate, and minimum principal stresses, respectively (Figure 1a). If pore fluid is present, the effective pressure $P_0 = P_c - P_f$, with P_f denoting pore fluid pressure. In this study, all of the deformation tests are conducted with a constant pore fluid (distilled water) pressure of P_f = 10 MPa. Sufficiently slow strain rates were used to ensure a fully drained condition during deformation [e.g., *Wong et al.*, 1997; *Baud et al.*, 2000]. At the preset confining pressure P_c in a conventional test, deformation is achieved by keeping the radial stresses constant ($\sigma_2 = \sigma_3 = P_c$), while advancing the axial piston to increase σ_1 at a constant displacement rate through a displacement servo control. Using this loading configuration, both the effective mean stress $P_{eff} = [(\sigma_1 + \sigma_2 + \sigma_3)/3 - P_f]$ and the differential stress $Q = (\sigma_1 - \sigma_3)$ increase concomitantly during deformation (Figure 1a).

[8] In contrast, under a lateral relaxation loading configuration, deformation is achieved by keeping the axial stress constant ($\sigma_1 = P_c$) while progressively decreasing the radial stresses σ_2 and σ_3 at a preset pace chosen to keep the strain rate comparable to that in the conventional test. Using such a loading configuration, the increase in differential stress Q is accompanied by a decrease in effective mean stress P during deformation (Figure 1a). Because the axial stress σ_1 is constant as the sample is deformed to failure, the increase in elastic energy stored in the loading frame is considerably less compared to that in a conventional test (Figure 1b).

[9] Mechanical data obtained using the new loading path are compared to those of the corresponding conventional tests. A representative set of stress-strain curves is shown in Figure 1c. Before yield-stress, the mechanical behavior of sample dd08 deformed at effective pressure P_0 = 190 MPa under lateral relaxation loading is in very good agreement with sample dd17 deformed at P_0 = 70 MPa using the conventional loading path. However, post-yielding inelastic behaviors of dd08 vs. dd17 demonstrate that the new loading configuration is effective in stabilizing the faulting process (Figure 1c). Note that to reach the same yield stress (i.e., identical P and Q values at the peak stress), the lateral relaxation loading is conducted at an effective pressure much higher than that used in the conventional test (Figure 1).

2.1. Sample Preparation

[10] Darley Dale sandstone samples with initial porosity of 13–18% were used in this study. Darley Dale sandstone was chosen because the mechanical and transport properties have been extensively studied under the conventional triaxial compression loading [e.g., *Read et al.*, 1995; *Wong et al.*, 1997; *Zhu and Wong*, 1997; *Baud et al.*, 2000; *Wu et al.*,

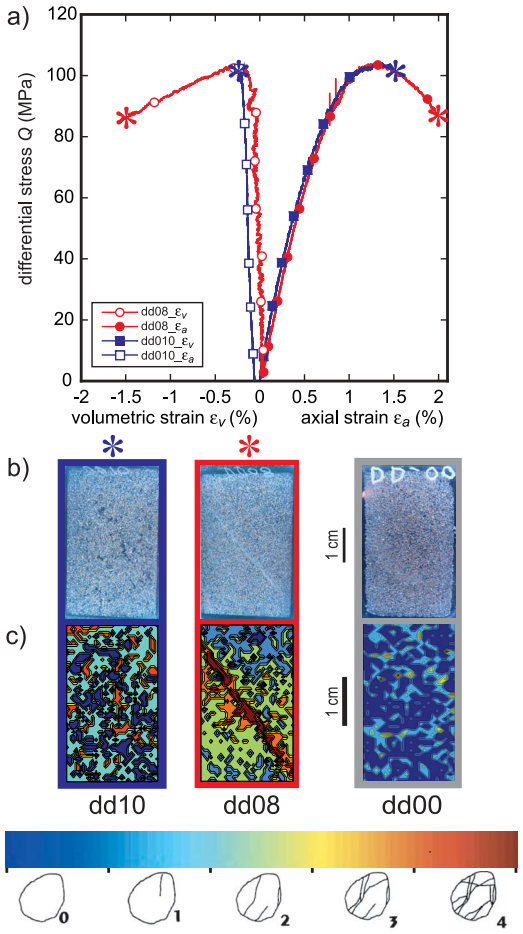

Figure 2. (a) Mechanical data of samples dd08 (red) and dd10 (blue), deformed at a nominal strain rate of 5×10^{-6}/s and an effective pressure of 190 MPa using the lateral relaxation loading. Both axial and volumetric strains as functions of differential stress are shown. Sample dd08 underwent a complete stress drop and a macroscopic shear fracture is developed, whereas sample dd10 was unloaded shortly after reaching the peak stress, no macroscopic shear fracture is visible. (b) Reflected light images of the thin sections of dd08 (red) and dd10 (blue). The actual width of these samples is 2.54 cm. Reflected light image of an undeformed sample dd00 is shown as reference. (c) Damage index maps of the thin sections dd08 (red), dd10 (blue) and dd00 (grey) are shown. The damage indices are developed by *Menendez et al.* [1996]. In the color map of the damage indices, blue represents grains with no microcracking (damage index = 0); cyan to green represents grains with 1 or 2 intragranular cracks (damage index = 1); green-yellow represents intact grain with more than 3 intragranular cracks, but no more than 2 transgranular cracks, i.e., cracks cutting the grain diametrically (damage index = 2); yellow-orange represents intact grains with more than 2 transgranular microcracks, but no obvious grain crushing (damage index = 3); red represents evident grain crushing (damage index = 4).

2000; *Heap et al.*, 2009]. For detailed petrophysical description of the sandstone, refer to *Wong et al.* [1997]. The samples were cored and ground to a cylindrical shape, with a diameter of 25.4 mm and a length of 50.8 mm.

[11] Before each test, samples were saturated with distilled water and jacketed with copper foil of 0.127 mm thick. Axial and circumferential strain gages were placed on the copper foil (Figure 1a). Jacketed samples were then positioned between two steel end-pieces, one of which had a concentric hole at the centre for fluid access to the pore fluid system. A programmable conventional triaxial deformation apparatus was used in this study, in which the confining pressure, axial load and pore fluid pressure can be independently servo-controlled using hydraulically powered intensifiers. All of the tests were conducted at room temperature. Failure mode in all deformed samples is brittle faulting.

2.2. Sample Series

[12] The first suite of experiments (dd series) consists of 2 samples with initial porosity of ~18%, dd08 and dd10 (Figure 2). Both samples were deformed at an effective pressure of 190 MPa and a nominal strain rate of $\sim 5 \times 10^{-6}$/s. During deformation, the effective mean stress decreases continuously and the differential stress increases to a peak value that marks the onset of progressive fault growth. The stress drop during fault propagation is sufficiently gradual that the deformation could be stopped anytime post-yielding. Indeed, sample dd08 was deformed until the faulting and stress-drop were complete; whereas dd10 was unloaded right after the peak stress was attained. Volumetric strain was calculated from the axial and circumferential strain gauge data. We follow the convention that shortening and volume reduction are positive, and elongation and volume increase are negative (Figure 2a). Excellent reproducibility of the mechanical data between dd08 and dd10 is observed (Figure 2a).

[13] The second suite of experiments (DDL series) consists of 4 samples with initial porosity of ~14%, DDL45, DDL46, DDL47, and DDL49. These samples were deformed at 3 different effective pressures P_0 = 80 (for DDL45), 150 (DDL46), 200 MPa (DDL47 and 49), respectively. Experimental details and comprehensive data including acoustic emission activity are published in *Zhu et al.* [2003]. For an easy reference, we compiled the stress-strain relations and porosity change in Figure 3a. The nominal strain rate used is $\sim 5 \times 10^{-5}$/s, an order of magnitude higher than the strain rate used in the dd series experiments. Pore volume change was recorded by a volumometer and porosity change was calculated from the pore volume change to the initial bulk volume of the sample.

[14] Deformed samples were cut in half along their axial axis. For deformed samples with visible macroscopic fractures, the cut was carefully placed along the longest dimension of the fault plane (Figures 2b and 3b). For samples with no apparent macroscopic fracture, the cut was placed based on visual examination of the damage at the ends of a sample where it is in contacts with steel end-pieces. Double polished thin sections of ~30 μm thick were then prepared (Figures 2b and 3b). For reference, a double polished thin section was also made for an undeformed sample dd00.

2.3. Crack Density Analysis

[15] Quantitative microstructural analysis was preformed on these thin sections using an optical microscope. To analyze the microscopic damage in the deformed samples, we followed the damage index developed by *Menendez et al.* [1996]. An index value of 0 represents a grain with no

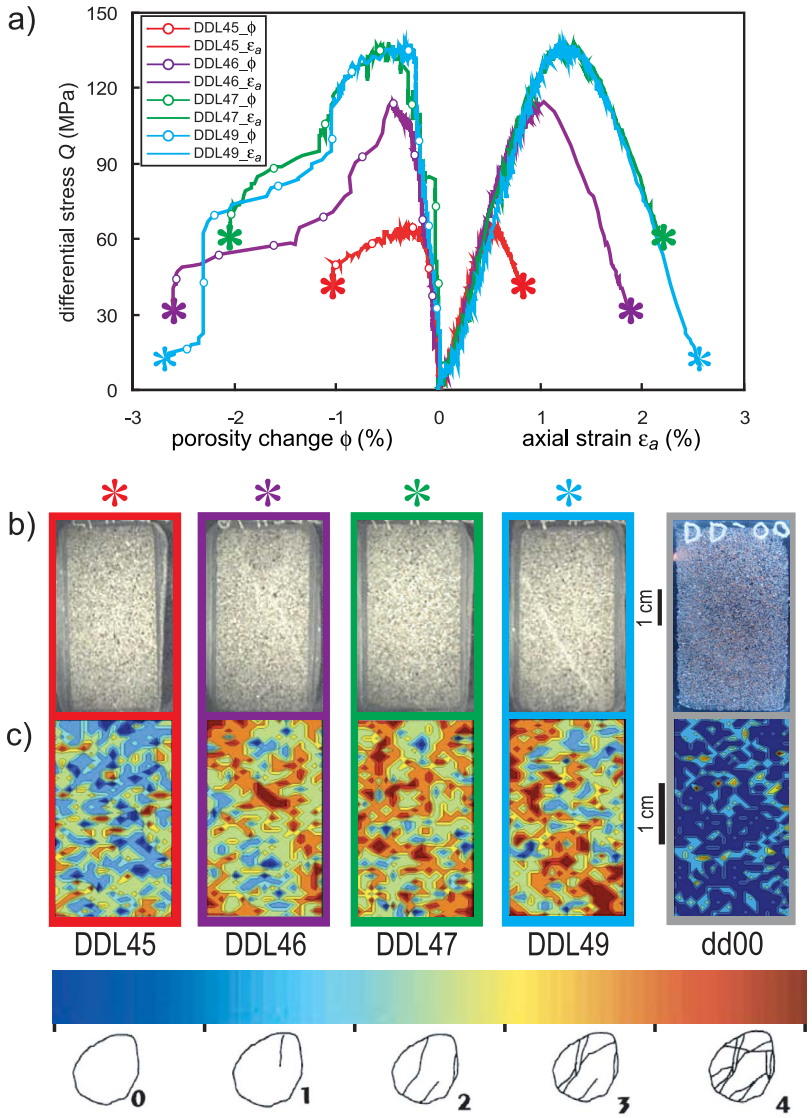

Figure 3. (a) Mechanical data of samples DDL45 (red), DDL46 (purple), DDL47 (green) and DDL49 (cyan) deformed at a nominal strain rate of 5×10^{-5}/s and effective pressures of 80, 150, 200, and 200 MPa, respectively, using the lateral relaxation loading. Both axial strain and porosity change as functions of differential stress are shown. (b) Reflected light images of the thin sections of DDL45 (red), DDL46 (purple), DDL47 (green) and DDL49 (cyan). The actual width of these samples is 1.84 cm. For reference, a thin section of an unformed sample dd00 (grey) is also shown. The actual width of the dd00 is 2.54 cm. (c) Damage index maps of the thin sections of DDL45 (red), DDL46 (purple), DDL47 (green) and DDL49 (cyan). For reference, a damage map of an unformed sample dd00 (grey) is also shown. The damage indices and color scheme for the damage map are identical to that used in Figure 2c.

visible damage in form of microcrack. Increasing in index values from 1 to 4 indicates higher microcrack density. An index value of 1 represents grains with 1 or 2 intragranular cracks. An index value of 2 represents grains with at least 3 intragranular cracks, but no more than 2 cutting through the grain diametrically (transgranular). An index value of 3 has at lease 2 transgranular cracks, but grain crushing is not evident. Maximum index value of 4 is assigned to visible grain crushing (Figures 2c and 3c).

[16] Damage index analyses were performed over the entire thin section for each sample. To present the distribution of microscopic damage within each deformed sample, we assigned each of these index values to a color spectrum, with dark blue to blue for an index value of 0, blue to cyan for 1, cyan to yellow for 2, yellow to red for 3, red and to dark red for 4. Using this convention, we produced a color-coded damage map of the deformed samples (Figures 2c and 3c). For example, in Figures 2c and 3c, the blue regions represent areas of no visible grain damage, and red regions indicate areas of grain crushing. For reference, damage index map of an undeformed sample dd00 is also shown.

3. Characterization of Microscopic Damage

[17] Reflected light images of thin sections made from the deformed samples dd08 and dd10 are shown in Figure 2b.

Sample dd08 was deformed at an effective pressure of 190 MPa and underwent a complete stress drop and sample dd10 was deformed at identical conditions but was unloaded right after peak stress (Figure 2a).

[18] A sharp shear fracture at angle of 39° to σ_1 is observed in sample dd08 (Figure 1). Damage index map of dd08 show that the maximum damage regions (with index values of 3 or 4) coalesce to form the macroscopic fracture. In comparison, there is no macroscopic fracture visible in sample dd10, and damage regions with an index value of 3 show no spatial correlation in dd10. This indicates that macroscopic fracture emerges after the peak stress, in good agreement with *Lockner et al.* [1992].

[19] The second set of samples were deformed at a faster strain rate (i.e., $\sim 5 \times 10^{-5}$/s), nevertheless qualitatively similar inelastic behaviors and microscopic damage were observed. While dilatancy and strain softening are observed in all 4 samples (Figure 3a), macroscopic fractures (with the rupture plane at an angle of 35°–37° with respect to σ_1) can only be clearly identified only in DDL46 and DDL49 (Figure 3b).

[20] DDL45, deformed at the lowest effective pressure of 80 MPa, has the lowest microscopic damage and no localized pattern is identified (Figure 3c). The peak stress of DDL45 is at $Q \sim 65$ MPa (Figure 3a). If deformed using a conventional compression configuration, an equivalent peak failure stress corresponds to deforming at an effective pressure P_0 between 5–10 MPa (Figure 1). At the same strain rate ($\sim 5 \times 10^{-5}$/s) under conventional loading path, unstable brittle faulting was observed in previous studies [e.g., *Wong et al.*, 1997; *Baud et al.*, 2000; *Wu et al.*, 2000; *Heap et al.*, 2009]. The contrast in failure modes shows that the amount of elastic energy release exerts a critical control in rupture stability.

[21] Note that samples DDL47 and DDL49 were deformed under identical conditions, with the only difference being that DDL49 underwent the complete stress-drop whereas DDL47 was unloaded after ~2/3 of the post-yield stress drop (Figure 3a). Compared to DDL49, the macroscopic fracture in DDL47 is much less visible. Together, DDL47 and DDL49 demonstrate the progressive fault growth under the lateral relaxation loading.

[22] Damage index maps of DDL47 and DDL49 show that microcracking is quite pervasive in both samples (Figure 3c). However, the crack density regions with an index value of 3 in DDL47 show a random spread over the entire sample, whereas the crack density regions with the same index value primarily concentrates along the eventual macroscopic fracture (Figure 3c). Our data confirms that microscopic damage becomes progressively more correlated during macroscopic failure growth, in agreement with the steepening trend of acoustic emission observed by *Lockner et al.* [1992]. Interestingly, the crack density regions with an index value of 4 in both DDL47 and DDL49 outline an emerging macroscopic fracture, indicating grain crushing is concentrated within the shear fracture (Figure 3c).

[23] The overall damage with an index value of 3 in DDL46 is visibly less than that in samples DDL47 and 49. This is consistent with the lower differential stress experienced by sample DDL46 compared to DDL47 and 49 (Figure 3a). Again, the crack density regions with an index value of 4 (grain crushing) is concentrated within the shear fracture in DDL46 (Figure 3c).

[24] While the initial porosity and grain size of the dd and DDL samples are somewhat different, modal analysis indicated that their compositions are very consistent (Figure S1 in Text S1 in the auxiliary material).[1] The mechanical behaviors also agree well among these samples, although the yield strength of the DDL samples are higher compared to the dd samples (Figure S2 in Text S1), likely due to the initial porosity and grain size difference [e.g., *Wong et al.*, 1997]. Comparisons of damage maps between the dd and DDL series imply that samples deformed at a slower strain rate (dd08 and dd10) suffer less overall microscopic damage. To some extent, the difference in initial porosity between the two suites of samples may also contribute to the observed difference in microscopic damage.

4. Concluding Remarks

[25] Due to the close relation between cracking induced dilation in rocks and the precursory phenomena that precede seismogenic faulting, it is important to understand the quantitative relationship between microcrack damage and macroscopic fault growth. We designed the so-called lateral relaxation loading configuration in which a cylindrical sample is deformed under decreasing radial stresses while the axial load remains constant. The failure process in samples deformed under the new loading path is stable enough so that deformation can be arrested at various stages during failure.

[26] A suite of porous sandstone samples were deformed and subsequently unloaded before or after macroscopic faulting occurs. Based on the quantitative characterization of microcrack density, we created damage index maps of each deformed samples to visualize the microscopic damage. Our data show that 1) before peak-stress, intragranualar cracking occurs throughout the deformed sample, with no special correlation, which is likely dictated by the distribution of the pre-existing defects; 2) after peak stress, microcracks coalesce and brittle fracture emerges; 3) in the brittle faulting regime, grain crushing is primarily associated with the macroscopic fault; 4) the extent and intensity of stress-induced microscope damage vary under different confinements and strain rates. Comparisons between these damage index maps provide an improved comprehension of the relationship between microscopic damage and macroscopic fracture development. The new loading path will also be useful in studying faulting in tectonic settings where the effective normal stress decreases as a result of elevated pore fluid pressure such as in accretionary wedges, where complex interplay between deformation and fluid flow takes place. Studies from Ocean Drilling Program documented a wide spectrum of failure modes from discrete faults to compaction bands [e.g., *Maltman et al.*, 1993]. To better understand the formation of these structures, new loading configurations closely tracking the actual stress path such as the one utilized in this study need to be considered in laboratory investigations.

[1] Auxiliary materials are available in the HTML. doi:10.1029/2012GL052487.

[27] **Acknowledgments.** Support for Tamarkin's thesis research came from the Department of Energy through grant DE-FG02-07ER15916. Partial support from the National Science Foundation through grant NSF-EAR1056317 is acknowledged. We are in debt to Phil Meredith who provided us the sandstone samples. Technical support from Ted Koczynski and Erich Scholz is greatly appreciated. Special thanks to Dave Olgaard, Chris Scholz, and Tom McMullen, who played important roles in building the Laboratory for Rock Physics at the University of Maryland. Reviews from an anonymous reviewer, Michael Heap, and Norm Sleep greatly improved the presentation of this work.

[28] The Editor thanks Michael J. Heap and Norman H. Sleep for assisting in the evaluation of this paper.

References

Baud, P., W. Zhu, and T.-F. Wong (2000), Failure mode and weakening effect of water on sandstone, *J. Geophys. Res.*, *105*, 16,371–16,389, doi:10.1029/2000JB900087.

Heap, M., P. Baud, and P. Meredith (2009), The influence of temperature on brittle creep in sandstones, *Geophys. Res. Lett.*, *36*, L19305, doi:10.1029/2009GL039373.

Jaeger, J., and N. G. Cook (1976), *Fundamentals of Rock Mechanics*, 2nd ed., pp. 179–181, Chapman and Hall, London.

Lockner, D., J. D. Byerlee, V. Kuksenko, A. Ponomarev, and A. Sidorin (1992), Observations of quasistatic fault growth from acoustic emission, in *Fault Mechanics and Transport Properties of Rocks*, edited by B. Evans and T. Wong, pp. 3–31, Academic, San Diego, Calif., doi:10.1016/S0074-6142(08)62813-2.

Maltman, A. J., T. Byrne, D. E. Karig, and S. Laaemant (1993), Deformation at the toe of an active accretionary prism: Synopsis of results from ODP Leg 131, Nankai, SW Japan, *J. Struct. Geol.*, *15*, 949–964, doi:10.1016/0191-8141(93)90169-B.

Menendez, B., W. Zhu, and T.-F. Wong (1996), Micromechanics of brittle faulting and cataclastic flow in Berea sandstone, *J. Struct. Geol.*, *18*, 1–16, doi:10.1016/0191-8141(95)00076-P.

Read, M., M. Ayling, P. Meredith, and S. Murrell (1995), Microcracking during triaxial deformation of porous rocks monitored by changes in rock physical properties, II. Pore volumometry and acoustic emission measurements on water-saturated rocks, *Tectonophysics*, *245*, 223–235, doi:10.1016/0040-1951(94)00236-3.

Reid, H. F. (1910), *The Mechanics of the Earthquake*, vol. II, *The California Earthquake of April 18, 1906, Report of the State Earthquake Investigation Commission*, *Carnegie Inst. Wash. Publ.*, vol. 87, edited by A. C. Lawson, 192 pp., Carnegie Inst. of Wash., Washington, D. C.

Scholz, C. (2002), *The Mechanics of Earthquakes and Faulting*, 2nd ed., Cambridge Univ. Press, Cambridge, U. K., doi:10.1017/CBO9780511818516.

Scholz, C. H., L. R. Sykes, and Y. P. Aggarwal (1973), Earthquake prediction: A physical basis, *Science*, *181*, 803–810, doi:10.1126/science.181.4102.803.

Terada, M., T. Yanagidani, and S. Ehara (1984), AE rate controlled compression test of rocks, in *Acoustic Emission/Microseismic Activity in Geological Structures and Materials: Proceedings of the Third Conference*, edited by H. R. Hardy and F. W. Leighton, pp. 159–171, Trans-Tech, Clausthal-Zellerfeld, Germany.

Wawersik, W., and W. Brace (1971), Post-failure behavior of a granite and a diabase, *Rock Mech. Rock Eng.*, *3*, 61–85, doi:10.1007/BF01239627.

Wong, T.-F. (1982), Shear fracture energy of Westerly granite from post-failure behavior, *J. Geophys. Res.*, *87*, 990–1000, doi:10.1029/JB087iB02p00990.

Wong, T.-F., C. David, and W. Zhu (1997), The transition from brittle faulting to cataclastic flow in porous sandstone: Mechanical deformation, *J. Geophys. Res.*, *102*, 3009–3025, doi:10.1029/96JB03281.

Wu, X. Y., P. Baud, and T.-F. Wong (2000), Micromechanics of compressive failure and spatial evolution of anisotropic damage in Darley Dale sandstone, *Int. J. Rock Mech. Min. Sci.*, *37*, 143–160, doi:10.1016/S1365-1609(99)00093-3.

Zhu, W., and T.-F. Wong (1997), The transition from brittle faulting to cataclastic flow: Permeability evolution, *J. Geophys. Res.*, *102*, 3027–3041, doi:10.1029/96JB03282.

Zhu, W., P. Baud, and T.-F. Wong (2003), Dilatancy and post-yielding behavior in porous sandstones: A new loading path, in *Soil and Rock America 2003: Proceedings of the 39th U.S. Rock Mechanics Symposium*, edited by P. J. Culligan, H. H. Einstein, and A. J. Whittle, pp. 437–444, Glückauf GMBH, Essen, Germany.